# Design of 1 arcmin resolution UHECR telescope with 50 degree angular diameter

M. Sasaki <sup>a,1</sup>, A. Kusaka <sup>b</sup>, and Y. Asaoka <sup>b</sup>

<sup>a</sup>Institute for Cosmic Ray Research, University of Tokyo, 5-1-5 Kashiwanoha, Kashiwa, 277–8582 Japan <sup>b</sup>Department of Physics, University of Tokyo, 7-3-1 Hongo, Bunkyo, Tokyo, 113–0033 Japan

(Dated: March 1, 2002)

#### **Abstract**

Based on the Baker-Nunn optics, we designed an optical system having an image resolution of less than  $0.02^{\circ}$  within the whole field of view of  $50^{\circ}$ . Combined with fine imaging devices with pixel size of  $0.02^{\circ} \times 0.02^{\circ}$ , the arrival directions of ultra high-energy cosmic rays and high-energy neutrinos can be determined with a superb accuracy of better than 1 arcmin. Crude knowledge of the ordered galactic magnetic field will permit the measurement of the atomic number of the cosmic rays if they are charged. Gamma rays or neutrinos can point directly back to the source object. The breakthrough in angular resolution will enable high energy particle observation to cooperate with and to be complementary to established astronomy using multi-wavelength of lights.

Key words: ultra high-energy cosmic ray; fluorescence detection; the Baker-Nunn optics; 1 arcmin angular resolution, wide field of view

#### 1 Introduction

The observation of ultra high-energy cosmic rays (UHECRs) and high-energy neutrinos (HE- $\nu$ 's) with the directional accuracy of  $\leq 1$  arcmin (') will make revolutionary progresses on particle astrophysics cooperating with traditional astronomical observations using multi-wavelength of lights. An excellent example is that the prompt observation of X-rays from GRB with the directional precision of 1' by Beppo-SAX made a crucial role of starting multi-wavelength observation with many advanced astronomical telescopes [1,2,3]. The directional accuracy of 1' is several tens times better

than that of  $\sim 1^{\circ}$  currently operating, constructing, or planning UHECR detectors [4,5,6,7] aim for.

Entering the atmosphere, UHECR produces an air shower (AS) by the interaction with air nuclei. The AS axis of UHECR accurately coincides with its incident angle, resulting in the intrinsic angular resolution below 0.3' at  $10^{17}$  eV. This is because (i) secondary particles are boosted by Lorenz factor of  $\sim 10^4$  toward the direction of the parent particle, and (ii) the transverse momenta of secondary particles hardly exceed 1 GeV/c as examined by the ATLAS group [8]. For UHECRs, more precise reconstruction of the primary direction is expected.

<sup>&</sup>lt;sup>1</sup> E-mail: sasakim@icrr.u-tokyo.ac.jp

AS can be detected via the isotropic fluorescence emission of the air nitrogen that it excites. An optical system with imaging devices can be used to track the longitudinal development of AS. This technique was first used by the Fly's Eye detector [9] and will be part of several future projects on UHECR detection. The good advantage of the fluorescence detection is the capability to reach a fine angular resolution. The signal to noise ratio (S/N) of each pixel of imaging devices is inversely proportional to the square root of the angular resolution. A better S/N will allow us to trigger and analyze lower energy and more distant events.

The galactic and extragalactic magnetic fields are considered to be roughly  $\mu G$  and below nG, respectively [10]. Thus, UHECRs are expected to be little deflected by the galactic and extragalactic magnetic fields, and cannot be confined by the galactic magnetic field. The existence of "ankle" at  $E \sim 10^{19}$  eV is often interpreted as a crossover from a steeper galactic component to a harder component of extragalactic origin.

Since possible sources of astrophysical accelerators which can produce UHECRs are very limited, little deflected UHECRs can be traced back to their sources. Thus, the excellent resolution of arrival direction will enable the cosmic-ray astronomy. The magnetic deflection of UHECRs during their propagation functions as the charge separator. One of the important implication of the 1' angular resolution is that the unambiguous particle identification can be performed using the deflection from sources. Furthermore, such observation might enable us to study the structure of extragalactic magnetic field.

Based on above scientific considerations, we propose achieving the telescope design with the field of view (FOV) of  $50^{\circ} \times 50^{\circ}$  and the 1' resolution of arrival direction. This will be realized by the combination of (i) a large area image intensifier (I.I.) connected to a CCD camera [11] and (ii) the Baker-Nunn optical system modified for our

purpose. In this paper, we will describe the conceptual design of the modified Baker-Nunn optical system. Assuming the image resolution of CCD camera is better than that of the optical system, expected performance of the telescopes for UHECR detection will be presented.

# 2 General Concept of Optical System

Our design requirements can be summarized as follows:

- (1) a large FOV of  $50^{\circ} \times 50^{\circ}$  to cover large solid angle for UHECR detection;
- (2) an image resolution of  $\sim 0.02^{\circ}$  to achieve the 1' resolution of arrival direction;
- (3) a large caliber with a diameter of  $\sim$ 2000 mm to distinguish faint fluorescence light.

In addition, cost performance will be a critical issue to construct a large-aperture array of telescopes.

Among several approaches to meat our requirements, the spherical mirror optics with an aperture diaphragm on the mirror's curvature center seems to have some suitable features for our purpose. This simple optics has the advantage of producing homogeneous images in the whole FOV. The typical aberrations which are presented off axis, principally the coma aberration, are eliminated, although the spherical aberration is not sufficiently small. Thus, we surveyed some variations of this optics. The candidates are the Schmidt, Makstov, Baker Super-Schmidt, and Baker-Nunn optics. Schmidt optics has one-element corrector lens at the diaphragm, and it realizes a better resolution than that without the corrector lens. However, we found that it was difficult to achieve the required image resolution over the wide FOV. Makstov and Baker Super-Schmidt optical systems require some thick corrector lenses, and thus they do not suit large-sized telescopes.

The Baker-Nunn optics has three-element corrector lens which consists of convex and concave lenses with spherical or aspherical surfaces [12]. The basic concepts of this optics are as follows: (i) each element has easy-to-make spherical surfaces, (ii) residual spherical aberration that remains after assembly is removed by altering the spacing between lens elements, and (iii) chromatic aberration can be eliminated by changing the lens materials. Figure 1 shows a schematic view of the Baker-Nunn optics. The second lens element is aperture diaphragm.

Although above-mentioned advantages are not directly connected to our purpose, three-element corrector lens in the Baker-Nunn optics provides a large degree of freedom for optimization. As a result, it can be most suited for our purpose. In our design, the diameter of first and third lens elements is 2400 mm, and the diameter of the second element is 2000 mm. The thickness of these elements is 10 mm. Considering the cost and fabrication processes, we designed the corrector lens as acrylic Fresnel lens to be appropriate for the large-aperture telescope. As described in the following section, the surface shape of each lens element is determined through optimization process.

# 3 Optimization using Ray Tracing

# 3.1 Ray Tracing

We developed ray-tracing program written in C++ in order to optimize the optical system and to examine its performance. In the program, refraction and reflection of incident rays on each surface are described, and thus bundle of on- and off-axis rays can be traced numerically. As is common in designing an optical system, the shape of the front

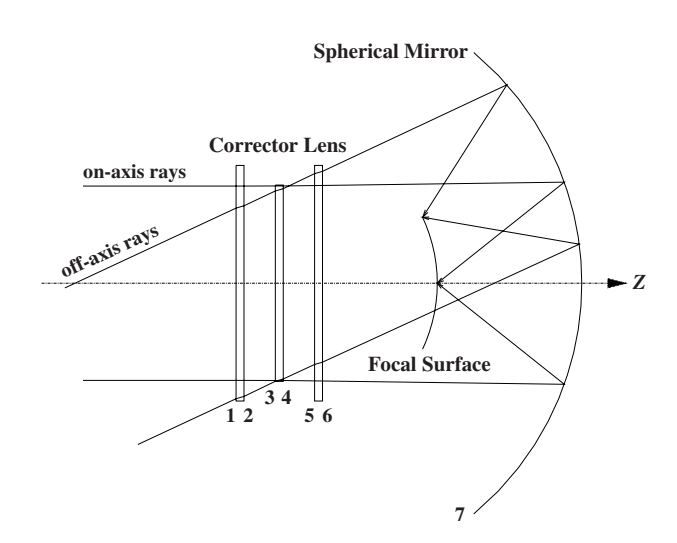


Fig. 1. Schematic view of the telescope based on the Baker-Nunn optics. The surfaces of each lens element and mirror are numbered from 1 to 7. The second lens element (3,4) is aperture diaphragm.

surface of each optical component is expressed as:

$$Z = \frac{h^2/R}{1 + \sqrt{1 - h^2/R^2}} + Ah^4 + Bh^6 + Ch^8, \tag{1}$$

where Z, h, and R represent the surface sag, radial height, and curvature of the surface, respectively. The sign of Z is positive toward the direction of on-axis incident rays. In addition, A, B, and C represent 4th, 6th, and 8th order aspheric coefficients, respectively. The surfaces of each lens element and the mirror are numbered from 1 to 7 as shown in Fig. 1.

The focal surface is defined by the condition of minimizing the image spot for a bundle of parallel rays. The spot size is defined as the root mean square (RMS) of positions of parallel rays at the focal surface. The fineness of a bundle of rays is determined for each purpose of the ray tracing, i.e., a rather rough interval between rays is selected for the optimization, and a fine interval is selected for the performance check. The spot size (s) is a function of the incident angle ( $\theta$ ) and the wavelength ( $\lambda$ ) of parallel rays.

# 3.2 Optimization

We used the modified Powell's method as the algorithm for the optimization with the following evaluation function:

$$F = \sum_{\theta} \left( \sum_{\lambda} s(\theta, \lambda)^2 \right)^2,$$

where  $\theta$  varies from  $0^{\circ}$  to  $25^{\circ}$ , and  $\lambda$  varies from 330 to 410 nm, taking into account the air-fluorescence emission spectrum. We adopted the fourth power of spot size as the evaluation function in order to obtain flat resolution all over the FOV.

In principle, the curvature, aspheric coefficients, thickness, and position of each lens element are all free parameters in optimization. In order to reduce the number of free parameters, we imposed the same symmetry as described in Ref. [12], i.e., the corrector lens is symmetric with respect to the plane which includes the center of the second element and is perpendicular to the axis of the ray. In addition, the thickness and position of each surface were fixed. These constraints enabled much efficient optimization. The resultant parameters of the optical system are given in Table 1. The axis and origin of Z coordinate are coincident with the axis of the rays and the center of the corrector lens, respectively. Note that we took into account the effect of the region obscured by the focal surface in the optimization.

Figure 2 shows the surface sag of some lens elements as a function of radial height. The surface sags remain well below 0.5 mm if we choose 10 mm as the width of Fresnel grooves. Thus, the 10-mm thickness of each lens element is sufficient, although the appropriate thickness may be changed according to the support method of the corrector lens. We confirmed that the same level of spot-size resolution can be obtained by another optimization if the thickness of each lens element

Table 1 Optimized parameters of the optical system.

1 1				
Surface	Z		Parameters	
1:	-405.0	R:	∞	
2:	-395.0	R:	-14767.2	
		A:	$2.30448 \times 10^{-11}$	
		B:	$-7.03756 \times 10^{-18}$	
3:	-5.0	R:	-30479.6	
		A:	$1.45344 \times 10^{-11}$	
		B:	$-6.37472 \times 10^{-18}$	
		C:	$-8.78219 \times 10^{-25}$	
4:	5.0	R:	30479.6	
		A:	$-1.45344 \times 10^{-11}$	
		B:	$6.37472 \times 10^{-18}$	
		C:	$8.78219 \times 10^{-25}$	
5:	395.0	R:	14767.2	
		A:	$-2.30448 \times 10^{-11}$	
		B:	$7.03756 \times 10^{-18}$	
6:	405.0	R:	∞	
7:	3082.0	R:	-3060.0	
·			(unit: mm)	

(unit: mm)

is changed.

Figure 3 shows the spot diagrams of the optimized optical system. The shape and size of spot diagrams change with the wavelength and the incident angle of the rays. As the wavelengths of diagrams, we select four largest fluorescence peaks at  $\lambda=336,358,391$ , and 425 nm, which dominate the filtered fluorescence light intensity after the propagation in the air. As for the incident angles,  $5^{\circ}$ ,  $15^{\circ}$ , and  $25^{\circ}$  are selected. The modified optical system improved the spot size of off-axis rays in compensation for that of on-axis rays.

Figure 4 shows the spot size distribution as a function of incident angle, taking account of the wavelength dependence of fluorescence light. Solid and dashed curves represent the spot size optimized to cover the FOV of  $\pm 25^{\circ}$  and  $\pm 20^{\circ}$ , respectively. The lens parameters shown in Table 1 are the re-

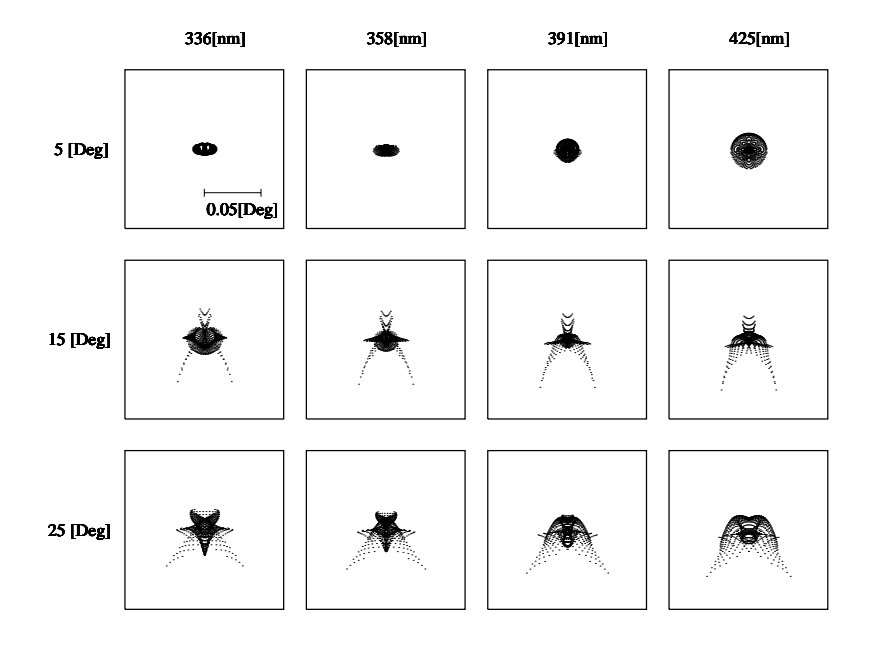


Fig. 3. Spot diagrams of the optimized optical system.

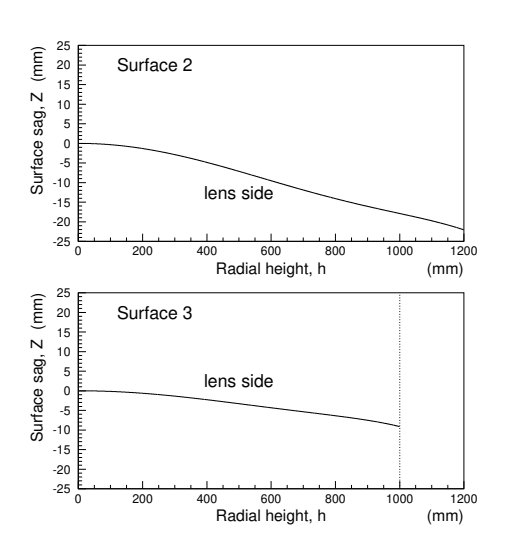


Fig. 2. Sag of the Surfaces 2 and 3 as a function of radial height. The each lens surface should be replaced by a series of concentric grooves to be a Fresnel lens.

sult of former optimization, and it achieves the spot size below  $0.02^{\circ}$  over the wide FOV of  $\pm 25^{\circ}$ . The results were confirmed by cross checks using Mathematica Optica [13] in which the refractive index of atmosphere was corrected.

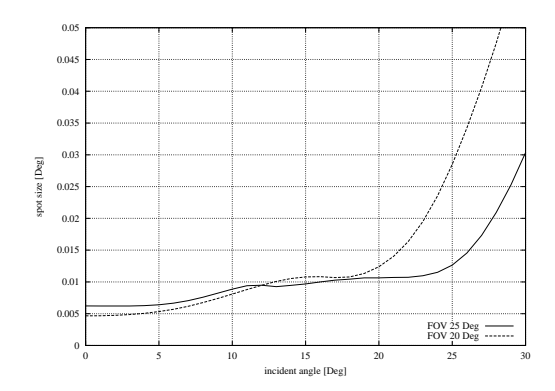


Fig. 4. The RMS distribution of the spot size as a function of incident angle, taking account of the wavelength dependence of fluorescence light.

Together with the development of the optical system, the fine-pixel imaging detector made by the large-area I.I. connected to a CCD camera has also been developed [11]. It was demonstrated in Ref. [11] that the pixel resolution of  $\sim 0.02^\circ$  was achieved. Combining the optical system with the imaging devices, the reconstruction resolution of the arrival direction will be discussed in the following section.

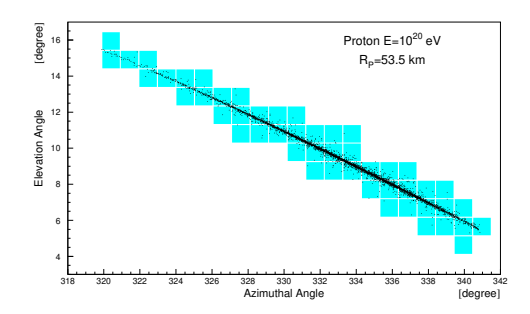
#### 4 Performance

By mounting the I.I.–CCD camera at the focal surface of the optimized optical system, the telescope is ready for UHECR detection. The solid angle of nearly  $2\pi$  sr can be covered by using 8 telescopes (denoted as a station), where 7 telescopes arranged azimuthally and 1 telescope directed upward. It should be noted that the telescope seeing upward is not significantly effective for UHECR detection, but for HE- $\nu$  detection [14].

In order to examine the resolution of the arrival direction of UHECRs, the Monte Carlo simulation was performed. The event generator calculates signal strength produced by atmospheric fluorescence light emission from AS with a given geometry, and builds simulation events by calculation of number of photoelectrons in every pixels of a CCD camera in each mirror. It involves the longitudinal and lateral profile of AS, the model of the atmosphere, the air fluorescence yield, and the detector optics. We took into account the fluctuations of the first interaction depth, impact point, and directional angles of shower cores with appropriate distributions.

Currently operating or planning fluorescence detector [5,7] has the pixel resolution of  $\sim 1^{\circ}$ . In order to compare the angular resolution of the reconstructed track between telescopes having  $0.02^{\circ}$ - and  $1^{\circ}$ -pixel size, we analyzed the same event samples which can be triggered by the  $1^{\circ}$ -pixel detector, i.e., we required (i) at least 6 pixels with  $1^{\circ}$  resolution were fired  $4\sigma$  above the night sky background, and (ii) the well reconstructed track which extended more than  $5^{\circ}$  in the FOV [5,7]. Note that the night sky background level of 100 photoelectrons/ $\mu$ s/( $1^{\circ} \times 1^{\circ}$ ) was assumed. Figure 5 shows the comparison of event displays between  $0.02^{\circ}$ - and  $1^{\circ}$ -pixel size.

Applying the stereo reconstruction of AS, the arrival direction is determined by the geometrical in-



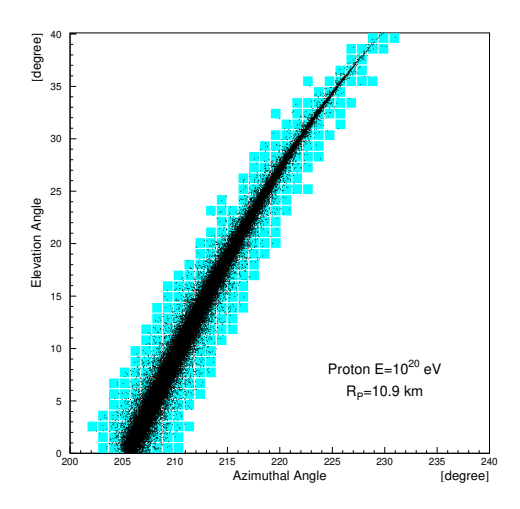


Fig. 5. Two examples of AS events for  $10^{20}$  eV protons. Top (Bottom) panel shows the events with  $R_{\rm P}=53.5$  (10.9) km, where  $R_{\rm P}$  means the impact parameter.

tersection of shower-detector planes (SDPs). Since the resolution of normal vector of SDP mainly contributes to the resolution of arrival direction, we discuss here for simplicity about the determination accuracy of SDP. The angular resolution of SDP determination is plotted in Fig. 6 for  $10^{19}$  and 10<sup>20</sup> eV protons. The angular resolution is determined from the integral distribution as the point below which 68 % of the events are contained. Figure 7 shows the energy dependence of the angular resolution of SDP. The excellent resolution of < 1' is obtained above  $10^{18}$  eV for SDP determination. In the case of stereo reconstruction with two or more stations, the pointing resolution is also expected to be  $\sim 1$ ' after the reconstruction of geometrical intersection of SDPs.

The S/N of each pixel satisfies the relation of  $S/N \propto (A/\Delta\theta)^{\frac{1}{2}}$  [9], where A represents the light

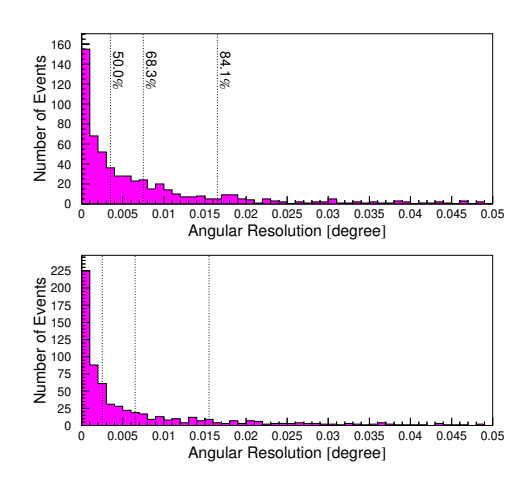


Fig. 6. The angular resolution of SDP for (Top)  $10^{19}$  and (Bottom)  $10^{20}$  eV protons.

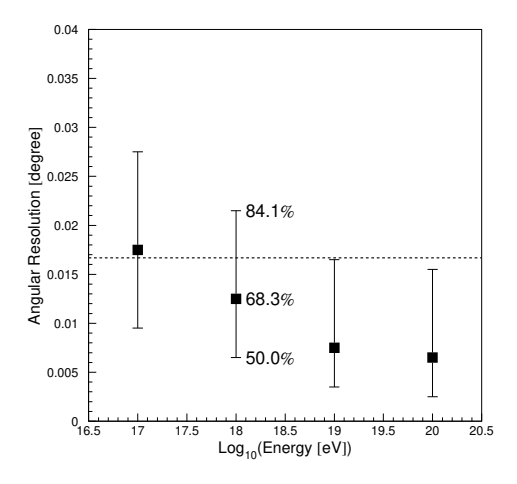


Fig. 7. The energy dependence of the angular resolution for SDP determination.

collection area, i.e., the reflection area for simple mirror optics and the area of aperture diaphragm for the Baker-Nunn optics, and  $\Delta\theta$  denotes the angular size of each pixel. Note that the relation is valid in the case of neglecting the effects of lateral distribution. Assuming the same size of A, the S/N value extracted from the  $0.02^{\circ}$ -pixel imaging device is expected to be about 7 times higher than that from the  $1^{\circ}$ -pixel one. To understand real effects from quantized number of photoelectrons, shape of AS profile, and so on, we examined quantitative improvement on S/N using the  $0.02^{\circ}$  pix-

els by the Monte Calro method. The AS events of protons with the energy of 10<sup>20</sup> eV were isotropically generated for a given impact parameter  $(R_{\rm p})$ . The maximum value of S/N (obtained event by event) is averaged at given  $R_p$ . Figure 8 shows the result of the simulation where the averaged S/Nmaximum for each AS is plotted as a function of  $R_{\rm p}$ . Note that event selection applied here is different from that applied to compare the angular resolution. The selection previously denoted as (i) is not required here to compare S/N of distant AS between the 1°- and 0.02°-pixel detectors. Open and solid squares represent the results with 1° and 0.02° pixels, respectively. The solid curve shows the expected S/N value calculated from that of 0.02° pixels using the above-mentioned relation. The expected and obtained S/N values are in good agreement for the distant events ( $R_p > 70 \text{ km}$ ). For the closer events, the size of shower-core image is not negligible comparing with that of 1° pixel taking into account the lateral distribution (see the bottom panel of Fig. 5). As a result, the expectation is sizably lower than the simulation result.

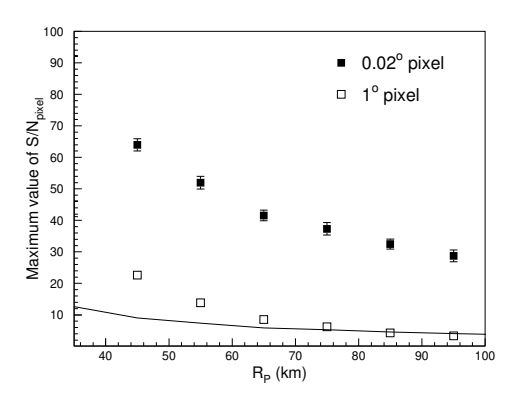


Fig. 8. Averaged maximum values of S/N for  $0.02^{\circ}$  and  $1^{\circ}$  pixels as a function of  $R_{\rm p}$  for  $10^{20}$  eV protons.

We define another signal to noise ratio  $(S/N_{\rm TRK})$  appropriate for track on the imaging devices. The signal (S) is the sum of charges detected by all pixels which are associated with the track. The background (BG) is also the sum of background for all pixels which are associated with the track.

Then,  $S/N_{\rm TRK}$  is defined by  $S/N_{\rm TRK} = S/\sqrt{BG}$ . Figure 9 shows the distributions of  $S/N_{\rm TRK}$  for protons of  $10^{19}$  and  $10^{20}$  eV. The open and filled histograms correspond to  $1^{\circ}$  and  $0.02^{\circ}$  pixels, respectively. Excellent values of  $S/N_{\rm TRK}$  were obtained for the  $0.02^{\circ}$ -pixel detector. Such a big improvement on  $S/N_{\rm TRK}$  was obtained because the lateral extent of AS is smaller than the pixel resolution of  $1^{\circ}$ . In addition to the better resolution of the arrival direction, the detailed performance of the detector such as the aperture, energy resolution, and shower-max resolution will be discussed elsewhere.

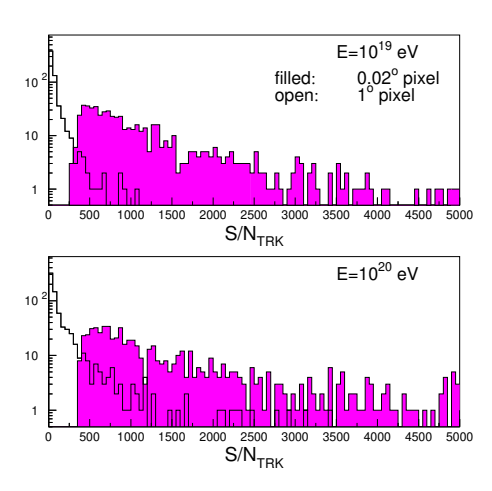


Fig. 9. Comparison of the  $S/N_{\rm TRK}$  between  $0.02^{\circ}$  and  $1^{\circ}$  pixels for (Top)  $10^{19}$  and (Bottom)  $10^{20}$  eV protons.

## 5 Conclusion

Based on the Baker-Nunn optical system, we presented the conceptual design of the new type of telescope for UHECR detection. The telescope has a spot size resolution below  $0.02^{\circ}$  within the whole range of the  $50^{\circ}$  angular diameter. We achieved the 1' angular resolution in the reconstruction of the arrival direction for UHECRs. Such a breakthrough in angular resolution will open the new sight in the field of UHECR and HE- $\nu$  physics.

## Acknowledgements

We would express gratitude to Y. Higashi for helpful advice and fruitful discussion. We appreciate continuous and various support by T. Aoki. We also thank N. Manago and M. Jobashi for their useful helps in the development of the Monte Carlo simulation.

#### References

- [1] E. Costa et al., Nature **387**, 783 (1997).
- [2] A. Yoshida et al., Publ. Astron. Soc. Jpn. 41, 509 (1989).
- [3] J.v.Paradijs et al., Nature 386, 686 (1997).
- [4] M. Takeda et al., Phys. Rev. Lett. **81**, 1163 (1998).
- [5] The High-Resolution Fly's Eye Experiment: http://hires.physics.utah.edu/; T. Abu-Zayyad et al., Astrophys. J. **557**, 686 (2001).
- [6] The Pierre Auger Project: Design Report, 2nd ed. March 1997, http://www.auger.org/.
- [7] The Telescope Array Project: Design Report, July 2000, http://www-ta.icrr.u-tokyo.ac.jp; M. Sasaki, Proc. of the EHECR2001, ICRR-Report-481-2001-11 (2001).
- [8] ATLAS Collaboration, ATLAS TDR 15, CERN/LHCC 99-15 (1999).
- [9] R.M. Baltrusaitis et al., Nucl. Instr. Meth. A 240, 410 (1985).
- [10] P.P. Kronberg, Rep. Prog. Phys., 325 (1994); P.P. Kronberg, Nature 370, 179 (1994).
- [11] M. Sasaki et al., ICRR-Report-485-2002-3 (2002).
- [12] J. Baker, "Correcting Optical System," U.S.Patent 3,711,184, 1962.
- [13] Mathematica Optica version 1.2.
- [14] M. Sasaki and M. Jobashi, ICRR-Report-484-2002-2 (2002).